HAXPES and laboratory XPS characterization of Pt and Ir oxyhydrate surface layers from anodized, polycrystalline Pt and Ir Foils

Benjamin Johnson, Chinmoy Ranjan, Mark Greiner, Rosa Arrigo, Manfred Schuster, Britta Höpfner, Mihaela Gorgoi, Iver Lauermann, Axel Knop-Gericke, Robert Schlögl

Abstract

Pt and Ir polycrystalline foils have been electrochemically oxidized through anodization to create thin platinum and iridium hydrous oxide layers and are analyzed with laboratory photoelectron spectroscopy during heating and time series (temperature programmed spectroscopy). The films contain oxygen in the form of a bound oxide, water and hydroxides which are investigated by depth profiling with high energy photoelectron spectroscopy. The Pt films are unstable and begin to degrade immediately after removal from the electrolyte, forming a core-shell structure with a metallic inner core and a hydrous oxide outer shell almost devoid of Pt. However, evidence of meta-stable intermediate states of degradation is found which offer possibilities for manufacturing PtO_x phases with increased stability. Heating the film to even 100°C causes accelerated degradation and shows that stoichiometric oxides such as PtO_2 or PtO are not the active species in the electrolyte. The Ir films exhibit increased stability and higher surface Ir content and gentle heating at low temperatures led to a decrease in electrically isolated surface states. Although both layers are based on noble metals, their surface structures are markedly different. The complexity of such hydrous oxide systems is discussed in detail with the goal of identifying film composition more precisely.

1. Introduction

Establishing new, alternative sources of energy is currently the topic of intense research around the world. Moving away from fossil fuels will lead to a multifaceted energy economy based on several kinds of renewable sources such as wind, solar and wave/tidal: technologies which have already made an impact on the world energy market.

One promising solution is the production of hydrogen through water splitting by electro-oxidation of oxygen in water. Common to all photochemical harvesting methods, this process is also found in living plants where oxygen and hydrogen are split via photosynthesis when light is absorbed in a leaf and charge (core-hole) separation occurs. The holes lead to the oxidation of water and production of oxygen by the oxygen evolving complex (OEC) in photosystem II with byproducts of electrons and protons. These then enter photosystem I and produce hydrogen in the form of NADPH through a ferrodoxin-$NADP^+$ reductase. Guided by the photosynthesis processes in plants, Daniel Nocera explores these ideas with his well-known artificial leaf [1] in the form of a solid state, wireless cell. Here a triple junction Si solar cell is sandwiched between an artificial OEC, self-assembled from cobalt, oxygen and phosphate and a hydrogen-evolving NiMoZn catalyst. As in photosystem II, the Co-OEC oxidizes water through a four-electron transfer mechanism. However, in contrast to nature which has developed healing mechanisms for its components, catalysts under real working conditions (open-flow systems) must exhibit high stability, especially during the oxygen evolution reaction, because they cannot self-heal. We note also that we do not consider re-precipitation to be a viable repair strategy [2].

Therefore, materials science attempts to develop not only efficient, but also stable catalysts. Simple models of these are based on TiO_2 and perovskite structures such as RuO_2 and IrO_2, although these theories do not consider the role of water in the catalyst structure. Further work requires not only identifying new materials, but also an understanding of the standard active catalysts themselves in terms of structure and electron transport, most notably PtO_x and IrO_x [3]-[9].

Although the actual goal is hydrogen generation, this reaction is dependent on a simultaneous oxygen evolution reaction (OER) which is the limiting factor in real systems. Research into this process hinges on understanding the mechanistic complexity of the 4-electron transfer and the corrosive nature of the OER which makes manufacturing suitable catalyst material challenging [10]. In this study we contribute to this task by analyzing the true active nature of OER catalyst systems using photoelectron spectroscopy to obtain compositional

data of the active materials PtO_x and IrO_x.

When grown anodically from precursor metallic foils, the result is a highly complex hydrous oxide film which has often been studied for both anodic oxygen evolution and cathodic hydrogen evolution. However, especially in terms of layer composition, many of the studies rely on simplified models in order to arrive at descriptions of the synthesized films. While a promising first step, more detailed studies must be completed to further refine our understanding, as an exact knowledge of film composition is a prerequisite to understanding the electronic dynamics through the layers and the interaction between oxygen and the catalyst at the active sites.

Here we attempt, through several different photoelectron spectroscopic methods, to illuminate the complexities of the Pt and Ir systems resulting from anodization including high-energy photoelectron spectroscopy (XPS) data for new insight into the depth profiles of such films. In addition, we scrutinize standard XPS data in order to extend our understanding beyond the usual interpretation and expand on our past studies [11]

2. Experimental

Both the platinum and iridium bulk hydrous oxide layers were formed by anodization of polycrystalline Pt and Ir metal foils, respectively. Polycrystalline foils are rich in defects, for example at grain boundaries, and can be oxidized more easily than single crystals.

The Pt samples were synthesized in 0.5 M H_2SO_4 at 2.5 V vs. reversible hydrogen electrode (RHE) while evolving oxygen. Under these conditions both Pt oxidation and oxygen evolution are significantly accelerated and the result is the growth of a pale brown film on the foil surface. The duration of synthesis varied according to the desired film thickness and was between one and two hours. Subsequent handling in air is unlikely to have had an oxidizing effect on the foil which was prepared under extremely oxidizing conditions. However,

turning off the applied potential may have resulted in chemical reduction.

The Ir samples were synthesized at room temperature under acidic conditions while cycling between 0 and 1.5 V vs. RHE. Known to be electrochromic, the Ir samples were removed from the electrolyte at 0 V vs. RHE (bleached). For the laboratory XPS measurements the sample was grown for 120 cycles, removed from the electrochemical cell and measured in the XPS chamber after differing durations in air (see Results and Discussion).

A more detailed description of the synthesis of the Pt samples as well as a complete electrochemical analysis is given in [12].

The resulting Pt and Ir samples are formed largely from bulk hydrous oxides of ill-defined stoichiometry and we have chosen the nomenclature $MO_x(OH)_y(H_2O)_z$, with M the metal component Pt or Ir, to describe them. The formula explicitly portrays the complexity of the films and leaves the stoichiometry in general terms as will be discussed later. The subscripts x, y and z in both Pt and Ir samples are not meant to denote any similarities in the respective stoichiometries and are chosen for convenience.

The laboratory XPS chamber used here has a base pressure of $\sim$8x10^{-10} mbar and is equipped with a Phoibos 150 MCD-9 hemispherical electron analyzer from Specs GmbH. Measurements were calibrated with Au $4f_{7/2}$ at 84.0 eV and Cu $2p_{3/2}$ at 932.7 eV. The high kinetic energy measurements were performed on the HIgh Kinetic Energy (HIKE) end station at the KMC-1 beamline at the Berlin Electron Storage Ring Company for Synchrotron Radiation (BESSY II) in Berlin, Germany using the Si (111) monochromator crystal and a SCIENTA R4000 high-resolution hemispherical electron anlyzer [13]. Quantitative XPS results were achieved by normalizing the fitted XP peaks with the number of scans, ionization cross-sections (taken from [14] for laboratory measurements and from [15] for HIKE measurements) and, in the case of the laboratory measurements, the transmission function of the electron analyzer. The mean free path of the photoelectrons was also taken into consideration although this quantity is strongly dependent on the unknown stoichiometry of the

sample.

3. Results and Discussion

$PtO_x(OH)_y(H_2O)_z$

Fig. 1 a) shows a typical XP survey spectrum (Mg Kα) of a $PtO_x(OH)_y(H_2O)_z$ bulk hydrous oxide film from an anodized polycrystalline Pt foil. Pt and O lines are evident along with S and N in small amounts from the synthesis process. b) shows a detail of the Pt 4f state measured with Mg Kα with the associated Pt 1 (often denoted Pt^0 or metal in the literature), Pt 3 (often denoted Pt^{2+}) and Pt 4 (often denoted Pt^{4+}) peaks, where we continue our nomenclature from Arrigo, *et al.* [11]. The fit parameters used are given in table 3 and show the quality of the fit: the peak binding energies and spin orbit splitting, ΔE, between the $4f_{5/2}$ and $4f_{7/2}$ components were fixed only for Pt 1 with the binding energy and ΔE of the Pt 3 and Pt 4 components allowed to vary. The table shows all three ΔE values to be similar as is expected.

We observed the Pt 1 peak within an hour of synthesis on layers 10s of nm thick meaning the Pt 1 (metal) signal does not originate from the metal substrate. Therefore, we infer the degradation of the oxidized foil begins soon after the completion of synthesis, although it has not yet been determined at which stage the degradation process begins. At the time of the measurement the atomic [Pt]/[O] ratio was 0.06 and will be discussed later with the HIKE results.

A test experiment shows that the appearance of the Pt 1 signal in fig. 1 b) is due to layer degradation found in thin layers and not from exposure to the X-ray source (beam damage). A Pt 4f photoelectron spectrum from a thick sample ($\sim$200 nm) prepared with the same synthesis found in the previous section but with a longer five hour anodization time is displayed in fig. 2. The longer oxidation time creates a surface PtO_2 layer with no Pt 1

(metal) component in XPS showing the sample to be stable during exposure to X-rays. The thicker sample is, however, unsuitable for further catalytic study because the surface layers have no direct contact to the oxide-metal foil interface and charge transport is reduced due to the thick PtO_2 layer. Further experiments were, therefore, performed with thinner Pt oxide layers.

A more detailed look at the impurities in the thin layers in figure 1 c) shows the S 2p measurement with peaks at 168.1 eV and 169.4 eV, indicating S present as thiosulfate and sulfate, respectively, while 1 d) shows the N 1s measurement with peaks at 401 eV and 399.2 eV indicating N present in the form of N-O and C-N-H compounds.

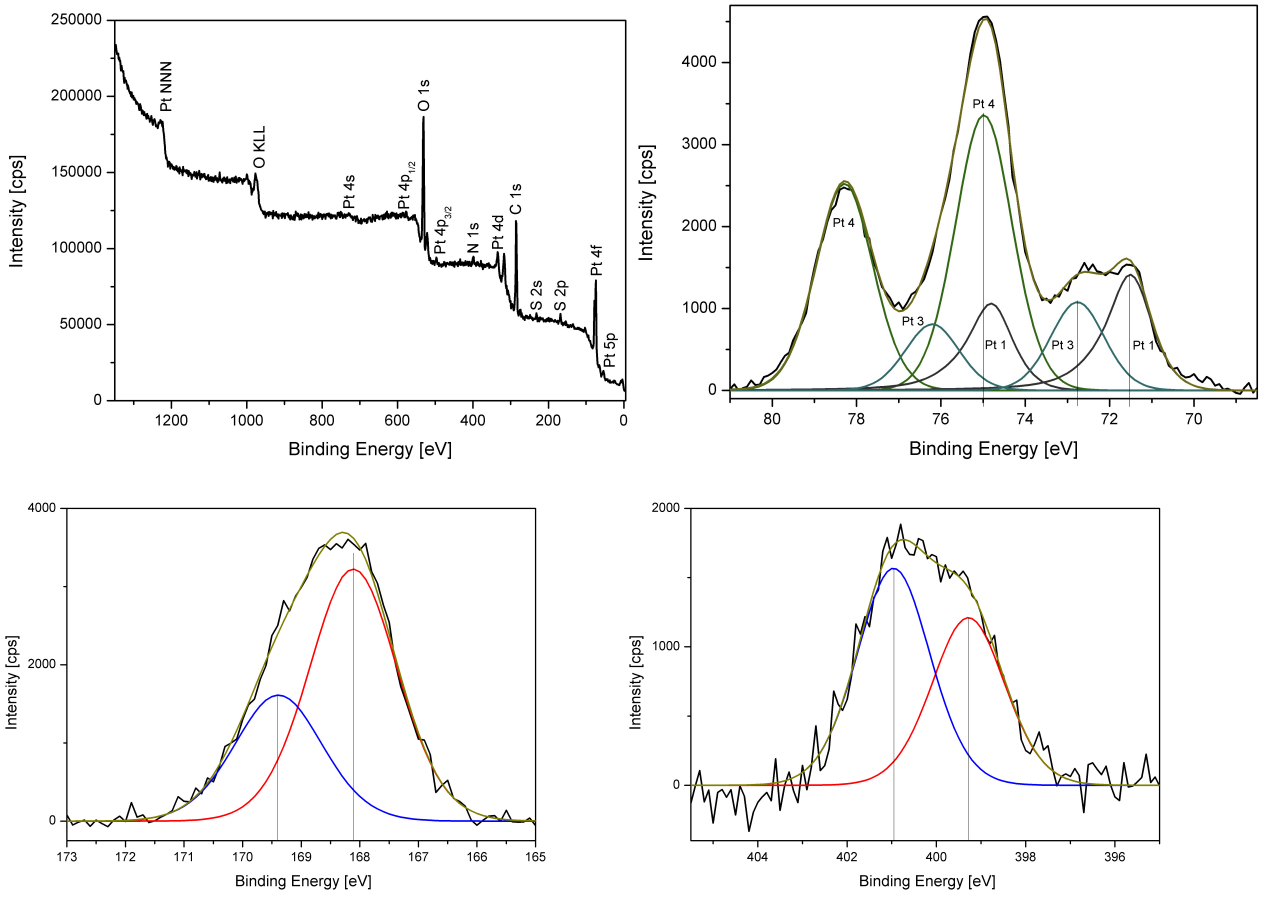

As a reference for the nomenclature found in the literature for both the Pt and Ir systems, table 2 contains often-cited publications with the initial discussions of Pt and Ir oxide films as well as several more current studies. Publications containing measurements sensitive to actual long-range order, for example EXAFS, are less common, although some can be found

FIGURE 1. a) Typical XP survey spectrum of $PtO_xOH_y(H_2O)_z$ showing the constituent elements of Pt, O, S and N. b) typical detail of Pt 4f (Mg Kα). Three peaks, Pt 1, Pt 3, Pt 4, are marked and correspond to the common literature nomenclature Pt^0 (metal), Pt^{2+} and and Pt^{4+}, respectively. The atomic [Pt]/[O] ratio was 0.06. c) S 2p spectrum showing contributions at 168.1 eV and 169.4 eV which indicate the presence of thiosulfate ($S_2O_3^{2-}$) and sulfate (SO_4^{2-}) species. d) N 1s spectrum showing contributions at 401 eV and 399.2 eV indicating the presence of N-O and C-N-H species. The traces of S and N are left from the synthesis process.

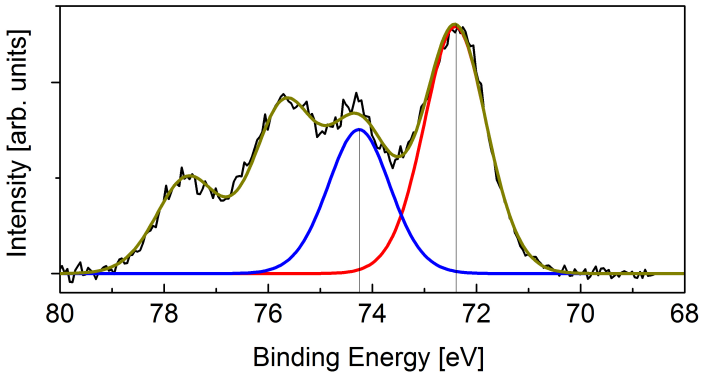

FIGURE 2. Pt 4f XP spectra from a thick (~200 nm) PtO_2 sample. The absence of a Pt 1 (metal) peak indicates stability of the oxide layer during exposure to X-rays. The presence of the Pt 1 peak in the thinner layers is, therefore, due to layer degradation and not the result of beam damage.

TABLE 1. Parameters used to fit the Pt 4f XPS spectra in this paper. The line shape in pro cent Gauss (G) and Lorentz (L) and possible asymmetry parameter, binding energy of the Pt $4f_{7/2}$ component, full width at half maximum (the same for the Pt $4f_{7/2}$ and Pt $4f_{5/2}$ components) and peak separation, ΔE, between 7/2 and 5/2 components are given.

	Pt 4	Pt 3	Pt 1
Line Shape	40% G, 60% L	40% G, 60% L	40% G, 60% L + asymmentry parameter
Binding Energy (Pt $4f_{7/2}$)	74.97 eV	72.64 eV	71.49 eV
FWHM	1.55 eV	1.71 eV	1.08 eV
ΔE	3.31 eV	3.32 eV	3.30 eV

[16]. Considering the O 1s peak in fig. 3 and that our method of synthesis lacks any thermal treatment, we hesitate to use the literature nomenclature, as the present system is surely of greater complexity than these labels reveal (perhaps even for the metal state). The O 1s signal does indeed contain contributions at the usual binding energies quoted for oxygen bound into an oxide phase (530 eV), hydroxides (531.8 eV) and H_2O (533.1 eV), the largest contribution appearing at energies near OH^- [17, 18, 19]. A key result is the low intensity

around 530 eV showing that only a small amount of the oxygen present in the sample is bound into an oxide and supports the low [Pt]/[O] ratio given above because most of the Pt is shown to be in oxide form in fig. 1 b). A possible method of full peak analysis can be found in [11]. We consider, therefore, the Pt (or Ir) atoms to be bound in an array of different local environments causing a broadening of the O 1s peak and 4f constituent signals grouped into the Pt 1, Pt 3 and Pt 4 peaks in fig. 1.

TABLE 2. Examples of current and past literature using common nomenclature of well-defined oxidation states in the PtO_x and IrO_x systems. "Basis" refers to the reasons for the chosen nomenclature in each study. For specific oxidation states and binding energies, please refer to the original article.

Publication	Year	System	Basis	Comments
W.N. Delgass, *et al.* [20]	1971	Pt, powder	Reference Materials	Does not contain anodized films
K.S. Kim, *et al.* [21]	1971	Pt, foil	Reference Materials	
G.C. Allen, *et al.* [22]	1974	Pt, foil	Citations	Uses "Oxide I" and "Oxide II" but discusses mainly Pt^{2+} or Pt^{4+} as possibilities. Discusses mixed $Pt(OH)+Pt(OH)_2$
J.S. Hammond, *et al.* [23]	1977	Pt, foil, polycr. plug	Citations	Uses "Oxide I" and "Oxide II" but discusses only Pt^{2+} or Pt^{4+} as possibilites. Cites controversy in literature.
M. Salmeron, *et al.*	1981	Pt, Ir Single Crystals		Uses LEED, AES to discuss proposed unit cell.
M. Peuckert, *et al.*[24]	1984	Pt, (111)	Reference Materials	
M. Peuckert [25]	1984	Ir, (111)	Reference Materials	Discusses only IrO_2 as possibility
J.B. Goodenough, *et al.* [26]	1988	Pt, powder	Citations	
L. Atanasoska, *et al.* [27]	1990	Ir, thermal decomp.	Citations	Discusses disagreement in literature
G. Lalande, *et al.* [28]	1999	Pt-Ru, powder	Citations	
B. Yang, *et al.* [29]	2003	Pt -Ru-C, powder	Citations	
R. Arrigo, *et al.* [11]	2013	Pt metal	New Nomenclature	This nomenclature is used in the current study

Further investigation on the stability and "oxide"-nature of the anodized layer was performed through a series of measurements with the sample subjected to temperature programmed XPS via electron beam heating from the backside of the sample.

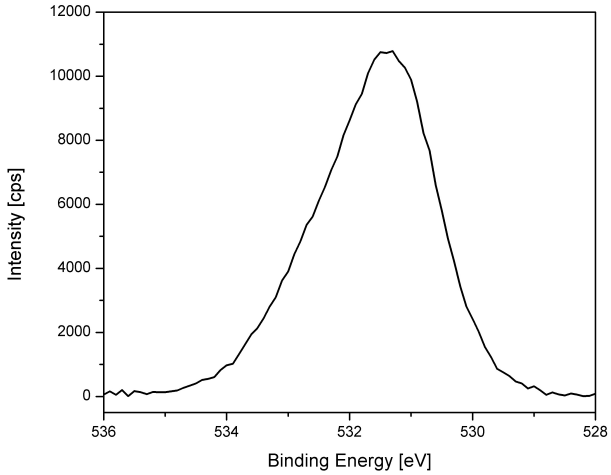

FIGURE 3. Detail of O 1s peak from the $PtO_x(OH)_y(H_2O)_z$ anodized film. Contributions to the spectrum can be found at binding energies 530 eV, 531.8 eV, 533.1 eV corresponding to oxygen bound into an oxide, hydroxides and H_2O, respectively. The small contribution at 530 eV shows most of the oxygen is not in oxide form.

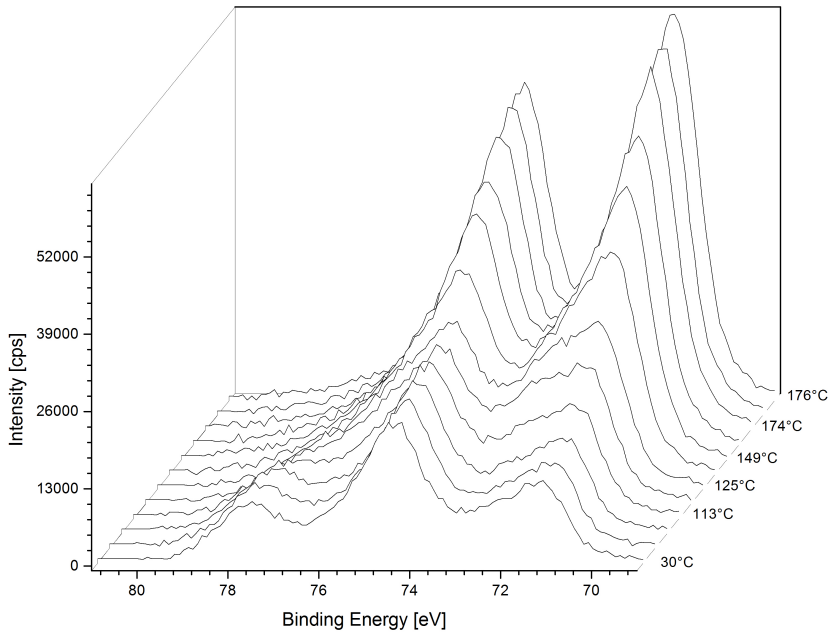

FIGURE 4. Heating series of $PtO_x(OH)_y(H_2O)_z$: rapidly measured Pt 4f detail spectra taken at the indicated temperatures. The change in signal intensity is indicative of the transition toward the metallic state and shows explicitly intermediate thermodynamic states. The degradation seen at low temperatures shows the initial state is not a stoichiometric oxide phase such as PtO or PtO_2.

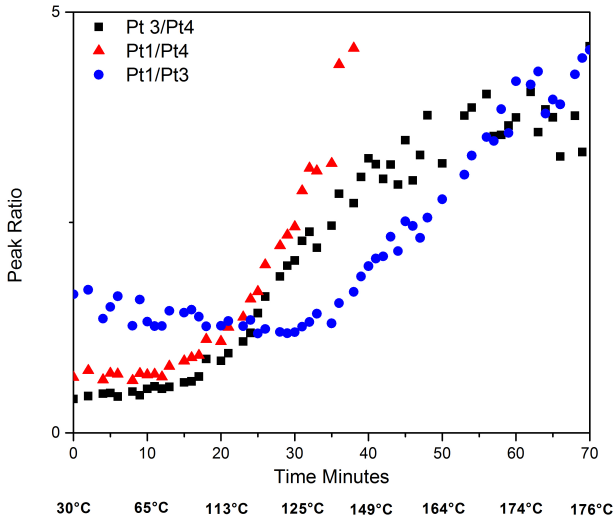

FIGURE 5. Graphical representation of the peak ratios from fig. 4. While the [Pt 1]/[Pt 4] and [Pt3]/[Pt 4] ratios rise from the beginning, the [Pt 1]/[Pt 3] ratio initially decreases before increasing. The given temperatures are only approximate and do not correspond exactly to heating time because the heating ramp was not linear.

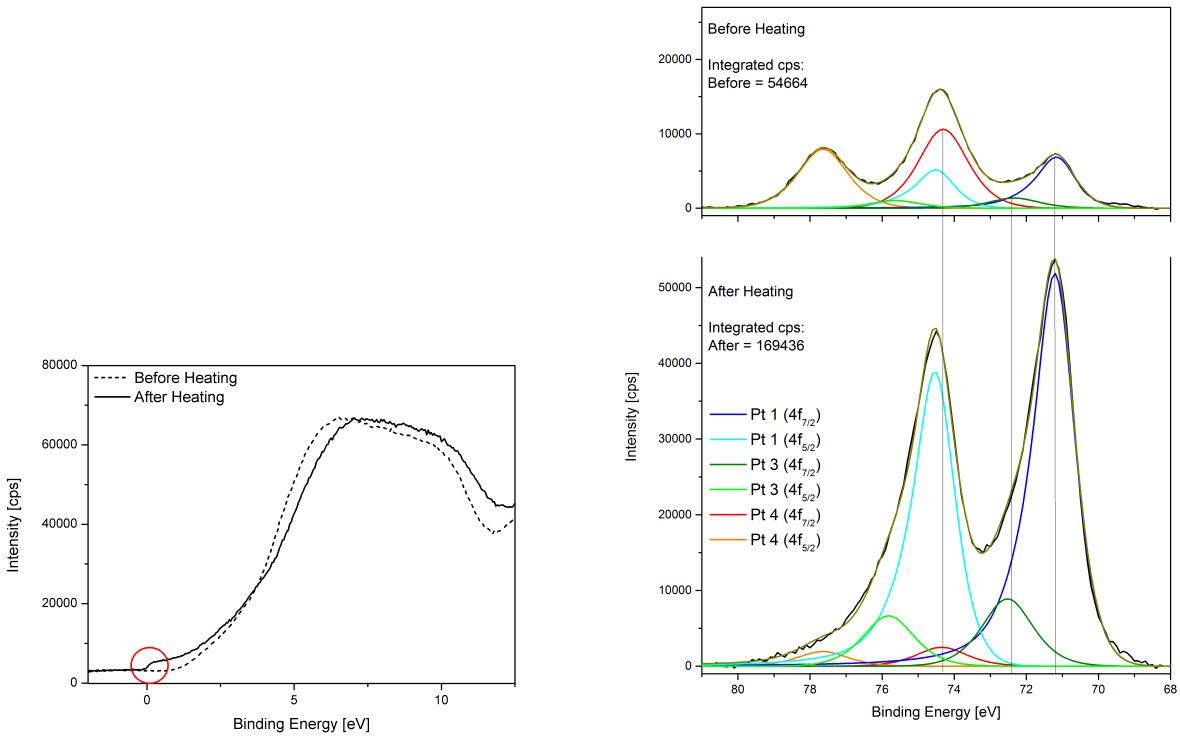

Fig. 4 shows rapidly measured Pt 4f spectra recorded at the indicated temperatures with a numerical representation of the peak ratios of the same in fig. 5. During heating many

FIGURE 6. a) He I valence band spectra before and after heating of $PtO_x(OH)_y(H_2O)_z$ showing the emergence of the Fermi Level. b) compares the Pt 4f detail spectra before and after heating. The change in signal intensity is indicative of the transition toward metal with intermediate states clearly visible.

intermediate states of as yet undetermined stability can be seen and will be discussed again further below. Fit parameters here are similar to table 3 but with slight variations to allow a satisfactory fit to the spectra of low intensity. The reduction of the Pt 4 peak at 78 eV shows the film begins to rapidly degrade at less than 100°C. The entire duration of the series is 71 min. For stoichiometric PtO_2 films we would expect stability up to about 200°C and even higher temperatures for PtO [32]. The original film, as discussed above, being reduced at such a low temperature in fig. 4, cannot be considered a stoichiometric oxide structure like PtO_2 or PtO. Furthermore, the sample has no defined temperature of decomposition as the component signals in fig. 4 change at different temperatures over intervals of minutes. The total change in the intensity of the Pt 4f peaks is indicative of the amount of surface area composed of Pt and shows a development toward the metallic phase. However, we have not yet determined whether the change is due to increased diffusion during heating or sample degradation. Fig. 6 a) shows the valence band spectra before and after heating. The shift of the d-band and emergence of a Fermi Level underscores the appearance of the metallic phase after sample degradation [25, 30]. It can be seen in fig. 6 b) that the surface of the sample was not completely reduced by heating in the vacuum. A clean Pt-metal reference using asymmetric peaks (not shown) was used to determine the exact form of the bare metal signal and is not sufficient here to fit the final state after heating in fig 6 b); additional peaks are needed to represent the remaining Pt 3 phase. This phase is more stable than the Pt 4 phase and leads, after heating, to a sample surface with a patchwork of Pt 1 and Pt 3 regions and illustrates the lateral inhomogeneity on the scale of the XPS measurement spot ($\sim$1 mm^2). The main initial degradation pathway here is Pt 4 $\rightarrow$ Pt 3 $\rightarrow$ Pt 1 as can be seen in figs. 4 and 5 with the initial growth of the Pt 3 signal relative to Pt 1. After about thirty minutes, this behavior reverses and the growth of the Pt 1 signal dominates. Despite the low expected conductivity of the material, the steady signals obtained in figs. 4 and 5

indicate no differential charging of the sample.

The investigation continues with experiments using a time series. Here, different sections (labeled 'a' through 'g') of an anodized Pt foil strip 5x20 mm in area were observed after differing times in air and in vacuum (fig. 7). "As Introduced" denotes samples introduced into the vacuum after being in air for the indicated time after synthesis and "Next Day" denotes the same sample after remaining in vacuum for an additional period after the "As Introduced" measurement was completed. Fig. 7 a) and b) show the Pt 4f detail spectra from samples 'a' and 'f' which represent measurements on extreme samples soon after synthesis and after an extended time in air, respectively (peaks have not been normalized). It is evident that the degradation follows the pathway in which most of the Pt 4 is reduced to Pt 3 while much smaller amounts of Pt 4 and Pt 3 are reduced to Pt 1.

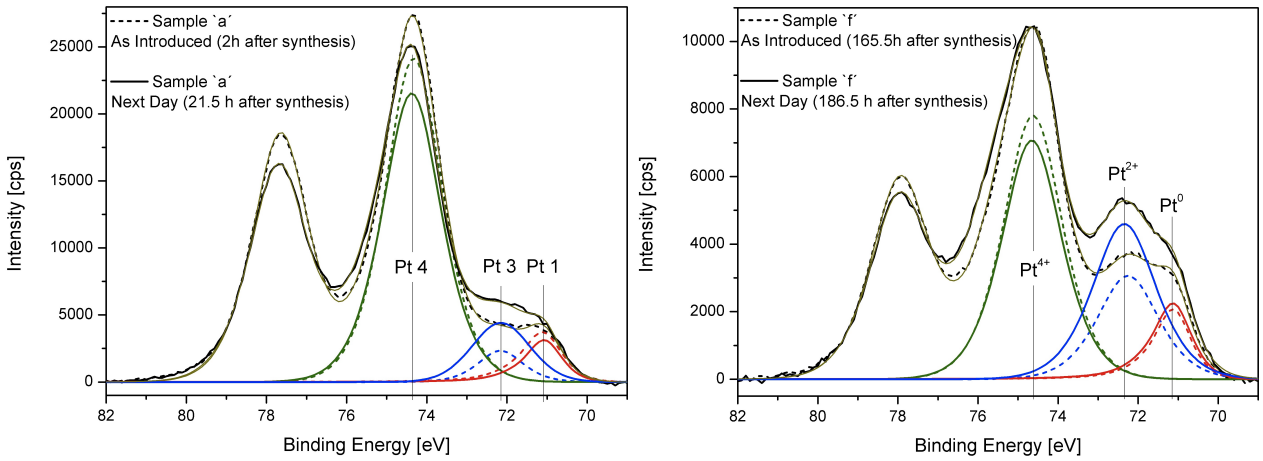

FIGURE 7. Time resolved degradation of $PtO_x(OH)_y(H_2O)_z$. a) shows the sample 'a' immediately after synthesis and after approximately 20 h in vacuum. b) shows the sample 'f' 165.5h hours after synthesis (in air) and after approximately 20 additional hours in vacuum. No peak normalization was performed.

The [Pt 3]/[Pt 4], [Pt 1]/[Pt 4] and [Pt]/[O] values for all samples ('a' through 'g') are found in fig. 8. The large spread in values evident in the graphical plot attests to the large lateral film variation occurring during film synthesis and the differing states of degradation present on the sample as well as locally differing, finite degradation rates. This important result shows that the intermediate states (also seen in fig. 4) through which the sample

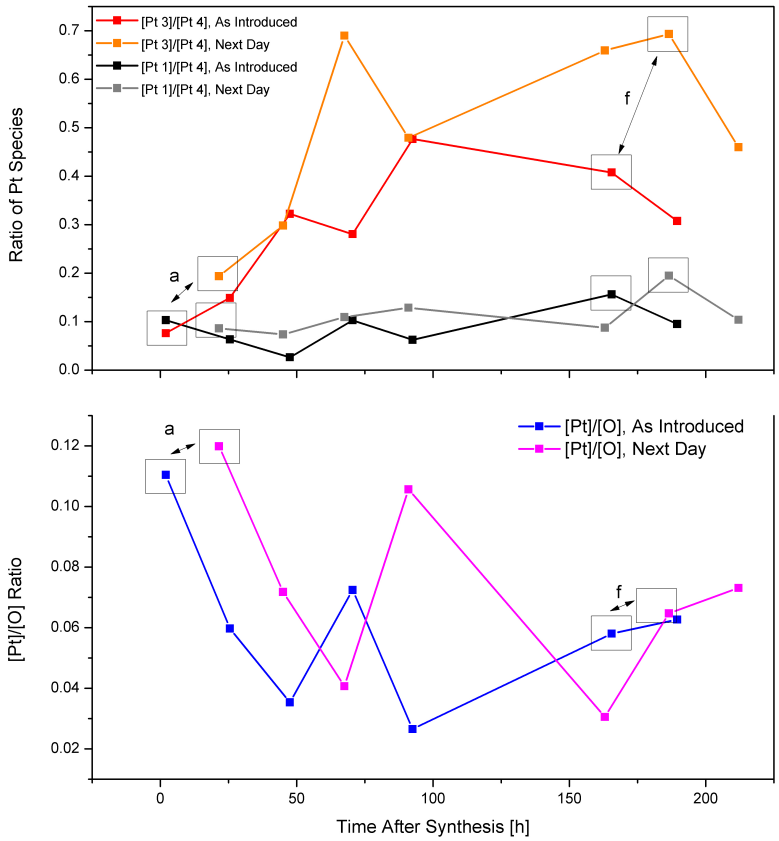

FIGURE 8. The [Pt 3]/[Pt 4] [Pt 1]/[Pt 4] and [Pt]/[O] ratios of the samples 'a' through 'g' are plotted graphically, both immediately after introduction into the vacuum chamber and from the succeeding measurement the next day (sample remained in vacuum). The increase in the [Pt 3]/[Pt 4] ratio is evident and is larger than the increase in the [Pt 1]/[Pt 4] ratio. The different degradation rates on the sample surface indicate the presence of intermediates states with some stability.

passes during degradation have some stability. If the intermediate states were transient, one would expect to see a homogeneous decay across all samples. Thus, it becomes possible in further experiments to identify meta-stable intermediate thermodynamic states, for example specific $[Pt_i]/[Pt_j]$ and $[Pt_i]/[O]$ ratios (i, j=1, 3, 4), with the hope of stabilizing them for use as durable catalysts.

The trend toward degradation of Pt 4 to mainly Pt 3 in fig. 7 c) is clear in every sample while the value of [Pt 1]/[Pt 4] increases much less. After 212 h the $PtO_x(OH)_y(H_2O)_z$ film still had not degraded to Pt 1, indicating the stability of the Pt 3 phase relative to the

Pt 4 phase which was also seen in the heating series. The main degradation pathway here is Pt 4 $\rightarrow$ Pt 3 and leaves the Pt 3 system in a meta-stable state. The discussion of the main degradation pathways in the heat and times series does not exclude the fact that other degradation processes or pathways may also be at work.

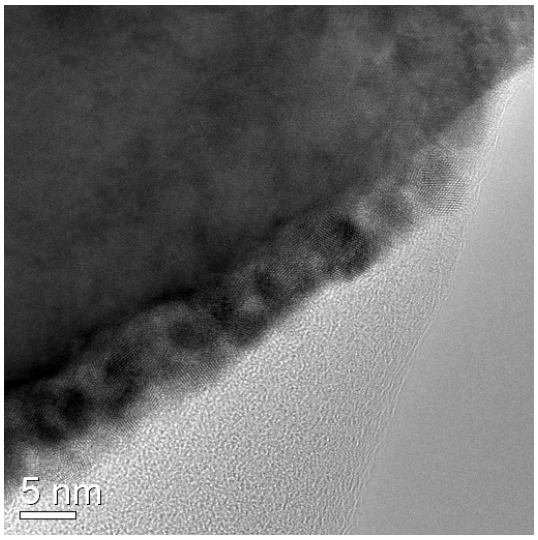

FIGURE 9. TEM image showing the $PtO_x(OH)_y(H_2O)_z$ film after the onset of degradation which results in spheres on the sample surface with a Pt 1 (metal) core and hydrous oxide outer shell. Note: this is not the same sample on which the XPS studies were performed.

The degradation process was also studied with depth-profiling. TEM images show the degradation of the anodized Pt films results in the formation of spheres of $PtO_x(OH)_y(H_2O)_z$ on the sample surface (fig. 9).[1] Energy dependent depth profiling at the KMC-1 beamline at the BESSY II synchrotron (Berlin, Germany) with the HIKE (HIgh Kinetic Energy) end station and angle resolved laboratory XPS measurements where used to determine the make-up of the spheres.

Fig. 10 shows the results of the HIKE depth-profiling measurements in a) spectrum and b) numerical form with the increase in both the [Pt 1]/[Pt 4] and [Pt 3]/[Pt 4] ratios clearly seen with increasing excitation energy. Here the atomic [Pt]/[O] ratios are also included in fig. 10 b) and can be divided into three regions as marked by the straight lines in the figure

[1]The XPS studies were performed on other samples. The TEM image is only for illustrative purposes.

and are discussed below.

As a reference for the HIKE results, we repeated the measurement at 2500 eV excitation energy at the end of the experiment. Because the film degrades quickly in vacuum, a test was needed to determine whether the changes seen in the high energy measurements (performed after those at lower excitation energies) were due to the film's degradation or to the higher information depth. Fig. 10 c) shows the Pt 4f signal at 2500 eV at the beginning (labeled "Start" in fig. 10 c)) of the depth profiling and the reference measurement performed at the end (labeled "End" in figs. 10 b) and c)). The Pt 3 component in the "End" measurement is larger than that of the metal which is typical of degradation (see the trend in fig. 7), while the high energy measurements show the metal component to be larger. Regarding bean damage (see discussion at the beginning of this section), we expect less here than in the laboratory measurements: at the high energies used at the HIKE beam line, the X-ray absorption cross sections are 1 to 2 orders of magnitude smaller than at surface sensitive energies (∼500 eV). Thus, although degradation during depth profiling is present, some of the increase in metal signal must derive from the higher information depth.

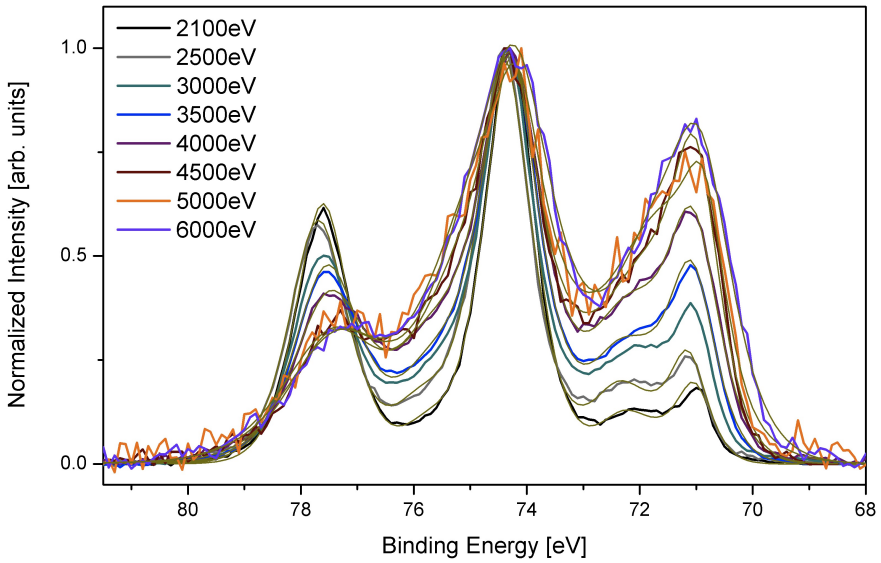

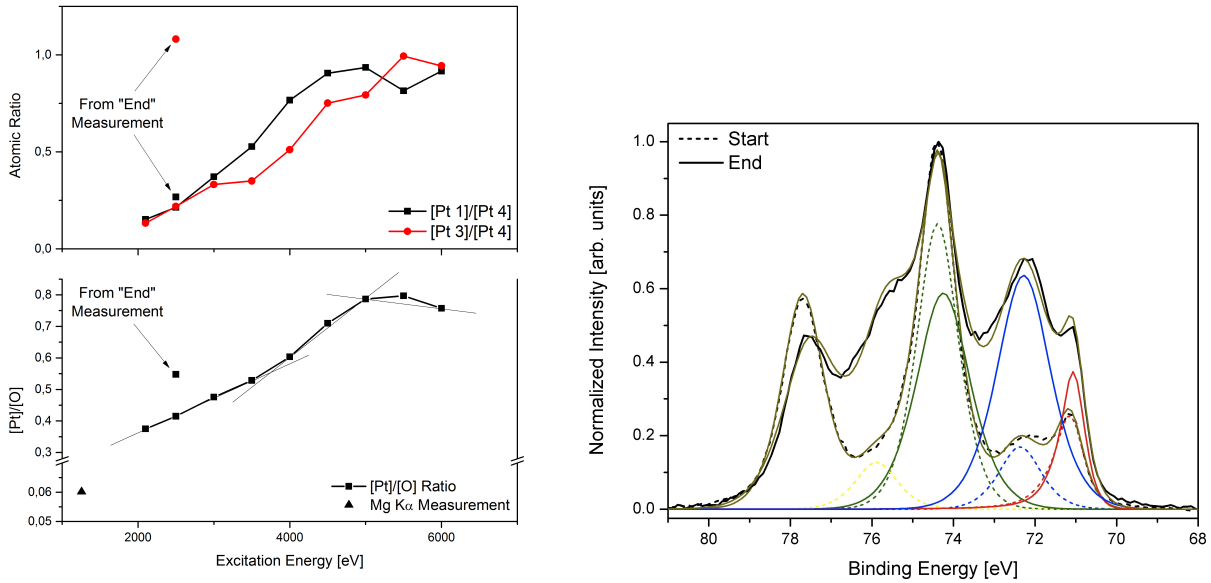

FIGURE 10. a) and b) depth profiling of the $PtO_x(OH)_y(H_2O)_z$ film showing an increase of the Pt 1 (metal) and Pt 3 signals with increased bulk sensitivity and atomic [Pt]/[O] ratios. c) the initial measurement at 2500 eV (labeled "Start") was repeated at the end (labeled "End") of the experiment to verify that the observed changes were due to the change in excitation energy (information depth) and not only sample degradation.

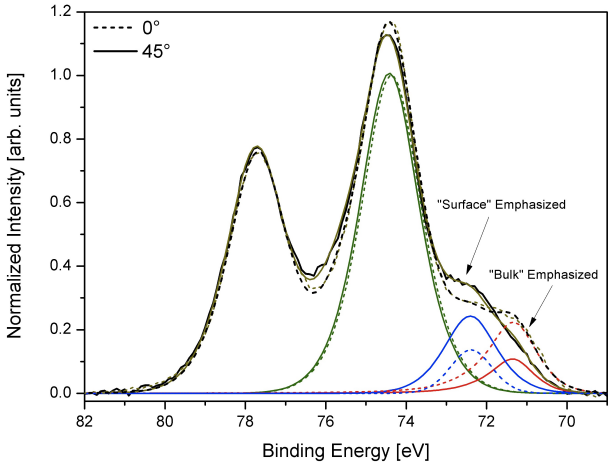

FIGURE 11. Angle resolved XPS measurement also showing an increase in the metal signal with increased bulk sensitivity.

In parallel to the HIKE measurements, angle resolved laboratory XPS measurements were also used to investigate stoichiometric changes with depth. The spheres on the sample surface in fig. 9 are 5-7 nm in diameter so that with Al Kα radiation a depth variation with angle may be expected. The results in fig. 11 show, as with the HIKE measurements, an

increase in Pt 1 signal with depth. However, here, the [Pt 3]/[Pt 4] decreases with depth in contrast to the HIKE measurements.

Considering both the HIKE and angle resolved measurements, the spheres appear to have a Pt 1 (metal) core and Pt 4 shell, although the exact position of Pt 3 in the structure remains ambiguous. Mixed between the core and outer shell, the Pt 3 phase may appear differently in experiments on different samples or at different points during sample degradation. Such a scenario describes the oxygen species leaving the center of the sphere, which is oxygen-depleted (metal), and diffusing outward, replenishing the oxygen that has already left the surface layers of the sphere. The three regions in the [Pt]/[O] ratio in fig. 10 b) are also consistent with a structure having a metallic core. Up to about 3500 eV the photoelectron signal penetrates deeper into the depth of the spheres shown in fig. 9 after which more of the substrate Pt metal is included in the measurement. After 5500 eV the signal starts to saturate as the [Pt]/[O] ratio changes slowly as only small amounts of additional Pt metal from the substrate are reached with higher excitation energies. The first region indicates a sphere size of ∼7 nm [31], slightly larger than the ∼5 nm) radius seen in fig. 9, although there may be some variation in sphere size from sample to sample. Finally, the inclusion of the [Pt]/[O] ratio from the Mg Kα measurement in fig. 10 b) shows the outer most layer contains a high amount of oxygen with a jump in the first several nm to a more Pt-rich composition. Thus, the outer termination layer may be almost completely devoid of platinum.

$\mathrm{IrO}_x(\mathrm{OH})_y(\mathrm{H_2O})_z$

Fig. 12 a) shows a typical XP survey spectrum of the $\mathrm{IrO}_x(\mathrm{OH})_y(\mathrm{H_2O})_z$ bulk hydrous oxide film.[2] Ir and O lines are evident along with N and S signals similar to those found in

[2]The use of the indices x, y and z are not meant to indicate any connection to the stoichiometry of the $\mathrm{PtO}_x(\mathrm{OH})_y(\mathrm{H_2O})_z$ discussed in the previous section. These commonly used letters are used again here only for convenience.

the $PtO_x(OH)_y(H_2O)_z$ films. b) shows a detail of the Ir 4f line measured with Mg Kα and includes a peak marked "Ir 4," found commonly in the literature as Ir^{4+}. A second component at a higher binding energy marked "Ir-D" is needed for a proper fit no matter the asymmetry of the Ir 4 peak and will be discussed below in terms of states electronically decoupled from the Fermi level. The asymmetry parameter of the Ir 4 peak was chosen because of the oxide's conductive nature and although the asymmetry could be an artifact stemming from several differing Ir oxidation states with similar binding energies in the hydrous oxide matrix. However, with no information about the binding energies of the other components, we have chosen to fit with an asymmetric peak. In contrast to $PtO_x(OH)_y(H_2O)_z$, the $IrO_x(OH)_y(H_2O)_z$ films are stable with no observed change in the XP spectra over time. However, like the Pt system, we refrain from using the nomenclature found in the literature for the same reasons cited earlier, including synthesis method, O 1s peak and instability to low heat exposure.

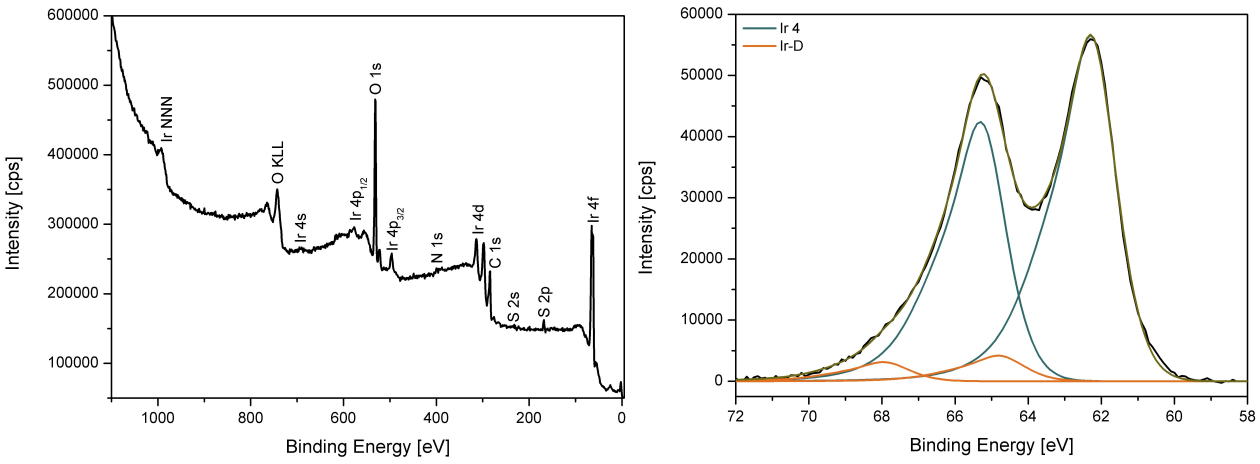

FIGURE 12. a) Typical XP survey spectrum of $IrO_x(OH)_y(H_2O)_z$ showing the constituent elements of Ir, O, S and N. b) typical detail of Ir 4f with Mg Kα radiation. Here a second component marked Ir-D is needed at higher binding energies to achieve a satisfactory fit.

The $IrO_x(OH)_y(H_2O)_z$ layer was investigated at BESSY II on the KMC-1 beamline with the HIKE end station. The results are shown in fig. 13 in both a) spectrum and b) graphical form with only the fitted Ir $4f_{7/2}$ components included.

TABLE 3. Parameters used to fit the Ir 4f XPS spectra in this paper. The line shape in pro cent Gauss (G) and Lorentz (L) and possible asymmetry parameter, binding energy of the Ir $4f_{7/2}$ component, full width at half maximum (the same for the Ir $4f_{7/2}$ and Ir $4f_{5/2}$ components) and peak separation, ΔE, between 7/2 and 5/2 components are given. The component "low oxidation state" applies to the HIKE measurements only.

	Ir 4	Ir-D	Low Ox. State
Line Shape	55% G, 45% L + asymmentry parameter	20% G, 80% L	40% G, 60% L
Binding Energy (Ir $4f_{7/2}$)	62.29 eV	64.08 eV	~64.5 eV
FWHM	1.63 eV	1.63 eV	
ΔE	3.04 eV	3.25 eV	~3.00 eV

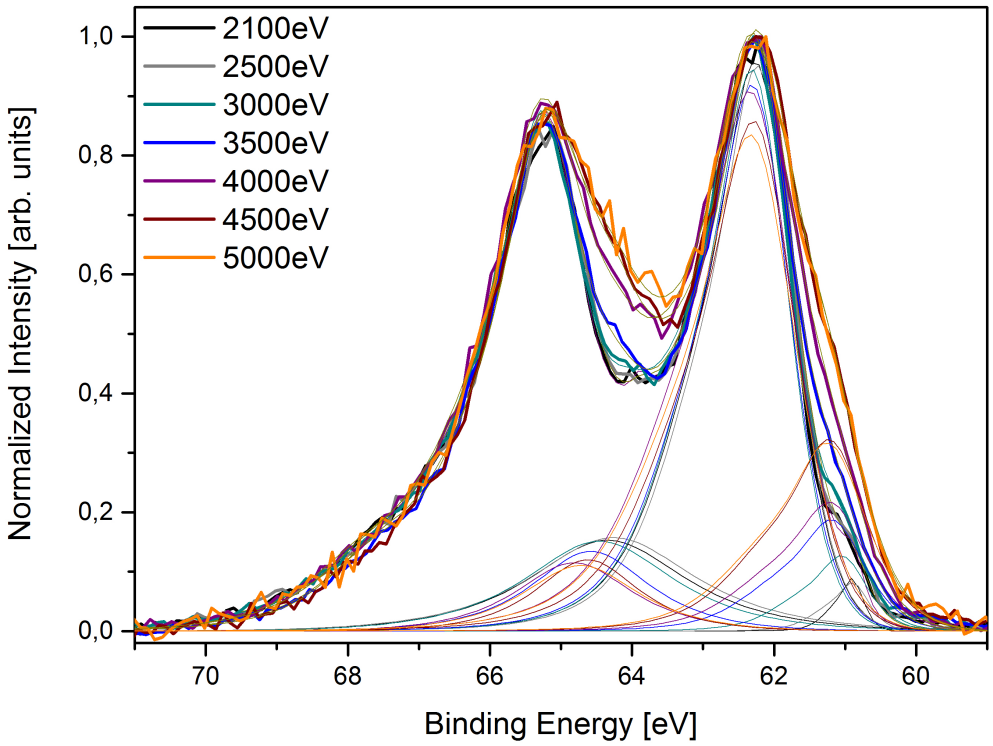

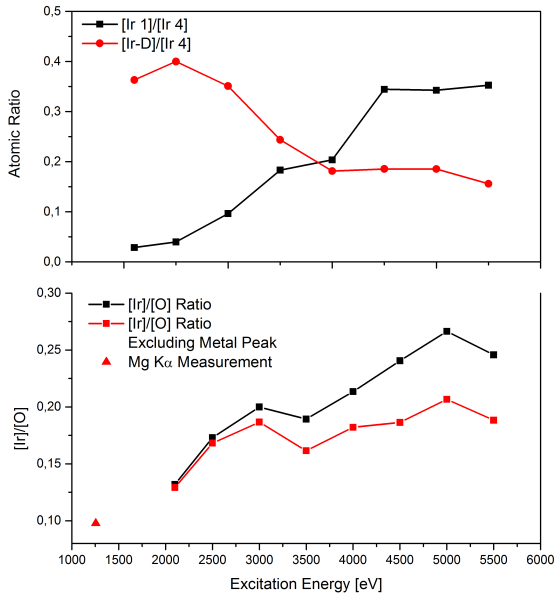

FIGURE 13. a) and b) depth profiling of the $IrO_x(OH)_y(H_2O)_z$ film with only the fitted Ir $4f_{7/2}$ component shown. Atomic [Ir]/[O] ratios are also given with and without the low oxidation Ir component at ∼61 eV labeled "Ir-1". The growth of this component is due to the increased signal information depth penetrating the core-shell structure.

A core-shell structure as seen in the $PtO_x(OH)_y(H_2O)_z$ samples can also be explained with this HIKE data. Beginning with [Ir-D]/[Ir 4] ratio, this value decreases with depth, showing the Ir-D component to be situated in the outer layers. Conversely, the rise in the value of the [Ir 1]/[Ir 4] ratio shows a lower oxidation state of iridium to be present in the core. Although this may indeed be Ir metal, we refer to this component as "low oxidation state Ir" because the floating nature (imprecise binding energy) in the fits in fig. 13 a) is too ambiguous to uniquely identify the metallic state. Part of this uncertainty is due to the broadening of the XP spectra at higher excitation energies, however, a definite structure in the spectrum (shoulder) on the low binding energy side of the Ir 4f spectra can be seen due to the presence of the low oxidation state Ir component. Considering the atomic [Ir]/[O] ratios, a possible core-shell structure is an outer shell of H_2O surrounding an $IrO(OH)_n$ layer with an IrO_2 layer inside of the that. The outer core consists of lower oxidation state Ir and finally a metallic Ir center. The HIKE measurements show the signal from the low oxidation state only becomes relevant at higher excitation energies (∼4000 eV). Corresponding to a depth of about 10 nm, this implies a core-shell structure diameter above 20 nm which is much larger than seen in the $PtO_x(OH)_y(H_2O)_z$ samples. This shows again that although both the Ir and Pt samples are based on noble metals adjacent in the periodic table, both resulting hydrous oxide layers behave differently.

The [Ir]/[O] ratios also show the outer layers of the Ir sample change less rapidly than the Pt sample, supporting the larger core-shell size. To emphasize this, the atomic [Ir]/[O] ratios are also shown without the deeper low oxidation state Ir component. The inclusion of the [Ir]/[O] ratio from the Mg Kα measurement in fig. 13 b) indicates that although the Ir sample is oxygen-richer than the Pt sample in the bulk, the outer 2 to 3 nm of the Ir sample contain a larger amount of metal than the Pt sample and have no jump in composition.

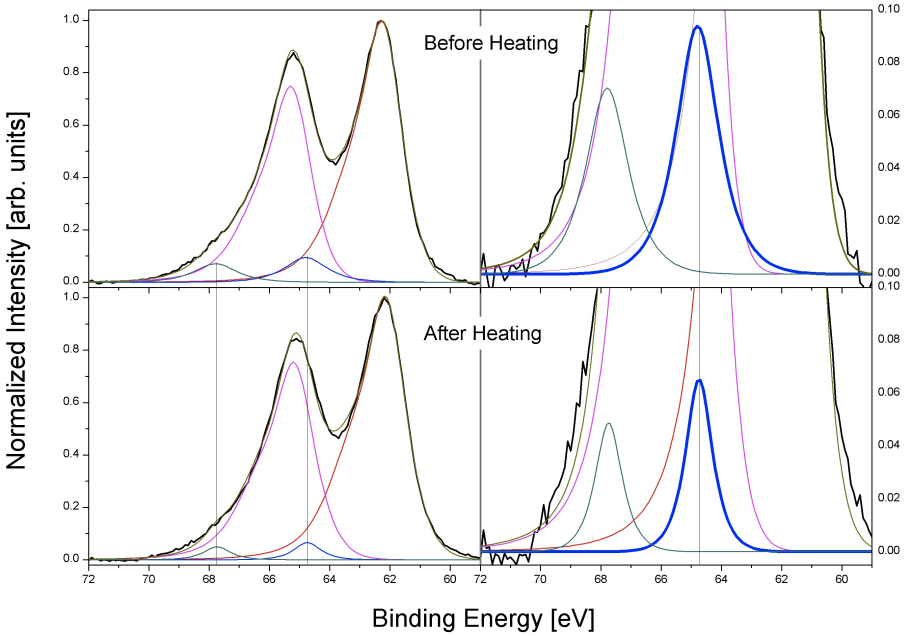

FIGURE 14. Al Kα spectra showing the decrease in the Ir-D component before and after heating of $IrO_x(OH)_y(H_2O)_z$ films. The change in the signal is attributed to increased electrical contact between surface islands and underlying film after water is evaporated.

Despite the low intensity of the Ir-D surface state, there is evidence that it is indeed real and not an artifact of the fit. Fig. 14 shows Al Kα measurements of an $IrO_x(OH)_y(H_2O)_z$ film before and after heating in vacuum to approximately 200°C for 30 sec. The position, form and FWHM of the peaks used for the fits remained the same before and after heating, only the size of the peaks was allowed to change. The Ir-D component is reduced in size by the heating when compared to the Ir 4 peak. Although a contribution from Ir in a higher oxidation state than Ir 4 would also result in such an XPS peak, in the absence of any evidence of this, we attribute this Ir-D to surface states (see the Ir HIKE results) which are electrically decoupled from the Fermi level. For example, small Ir islands isolated electrically from the rest of the film by a water layer which are shifted due to differential charging in the XP spectrum. Heating causes a reduction of the insolating water layer through evaporation and, thus, also in the measured signal of the Ir-D component. Although the choice of a symmetric Ir-D peak for fitting is arbitrary, the fit shape emphasizes more clearly the reduction of the high binding energy shoulder of the spectrum after heating. The samples are, therefore, not composed of a stoichiometric IrO_2 phase as this remains stable in vacuum up to ~570°C [33].

For RS to supplement:

Discussion of healing mechanism for Ir-D component.

–and–

Chemical discussion of core-shell model and different behavior of noble metal-based hydrous oxides + graphic.

4. Conclusion

Pt and Ir metal foils were oxidized through anodization resulting in complex Pt and Ir hydrous oxide layers. XPS measurements were similar to those found in the literature in the prior four decades, however, here we emphasize that the spectra contain no direct information about the phases present in the films and real information about short or long-range order must be gathered from other experiments.

Although both samples are based on noble metals, the resulting anodized layers differed in several respects.

The $PtO_x(OH)_y(H_2O)_z$ layer degraded after synthesis forming surface core-shell structures with a metal core and Pt 4 outer shell, the termination layer of which contains almost no Pt. The degradation process was different depending on whether the sample was heated (Pt 4 $\rightarrow$ Pt 3 $\rightarrow$ Pt 1 pathway) or left to degrade in air (Pt 4 $\rightarrow$ Pt 3 pathway). The low heat needed to accelerate degradation indicates the absence of any actual extended regions of stable, stoichiometric PtO or PtO_2 phases. Also, samples made simultaneously on a single piece of foil had large lateral variations in composition. This points to the existence of non-transient intermediate states with finite lifetimes.

In comparison, the $IrO_x(OH)_y(H_2O)_z$ films degraded less with time and had a higher metal content in their outer layers. The photoelectron spectroscopic data from these layers can also be interpreted with a core-shell model with highly oxidized outer layers and a metallic inner core, although the structures are larger than on the surface of the Pt layers. The small changes in the Ir 4f XP signal seen during heating can be explained in terms of increased electrical connection between surface and film leadin to a reduction in the the high binding energy shoulder of the spectrum.

Future experiments will expand on this work by concentrating on measurements more sensitive to physical surface structure and chemical environment (EXAFS, NEXAFS) in an attempt to identify the intermediate thermodynamic states seen during degradation (fig. 4). In order to successfully identify suitable catalytic layers, materials science must understand the complex kinetics of degradation in order to stabilize these intermediate states. Differences seen *in-* and *ex-situ* as well as between samples exposed to air and those kept in anaerobic environments before being loaded into the vacuum chamber will enable conclusions to be drawn about catalysts in active states and the effects on a system from different measurements methods. The importance of this step is underlined by the often *ex-situ* nature of the spectroscopic methods used in this study. This will build a strong basis data set for future experiments at the EMIL beamline at BESSY II in Berlin.

Acknowledgements: We thank the Helmholtz-Zentrum-Berlin (Electron Storage Ring BESSY II) for providing synchrotron radiation at the KMC-1 beam line.

References

[1] D. G. Nocera, Acc. Chem. Res., **45**, 767-776 (2011)

[2] H. Kasai, H. S. Nalwa, H. Oikawa, S. Okada, H. Matsuda, N. Minami, A. Kakuta, K. Ono, A. Mukoh, H. Nakanishi, Jpn. J. Appl. Phys., **31**, L 1132-L 1134 (1992)

[3] H. Yamazaki, A. Shouji, M. Kajita, M. Yagi, Coord. Chem. Rev., **254**, 2483-249 (2010)

[4] M. W. Kanan, D. G. Nocera, Science, **321**, 1072-1075 (2008)

[5] H. J. M. Hou, Journal of Integrative Plant Biology, **52**, 704-711 (2010)

[6] H. Dau, C. Limberg, T. Reier, M. Risch, S. Roggan, P. Strasser, ChemCatChem, **2**, 724-761 (2010)

[7] N. Lewis, D. G. Nocera, P. Natl. Acad. Sci. USA **103**, 15729-15735 (2006)

[8] R. Schlögl, ChemSusChem , **3**, 209-222 (2010)

[9] N. I. Shutilova, D. N. Moiseev, Prot. Met. Phys. Chem. Surf., **46**, 502-507 (2010)

[10] N. Alonso-Vante, B. Schubert, H. Tributsch, Mat. Chem. Phys., **22**, 281-307 (1989)

[11] R. Arrigo, M. Hävecker, M. E. Schuster, C. Ranjan, E. Stotz, A. Knop-Gericke, R. Schlögl, Ang. Chem., **125**, 11874-11879 (2013)

[12] C. Ranjan, R. Arrigo, M. E. Schuster, R. Schlögl, M. Eiswirth, B. Johnson, F. Girgsdies, G. Weinberg, A. Knop-Gericke, J. Tornow, Some Journal **Vol.** 0000-9999 (2014)

[13] M. Gorgoi, S. Svensson, F. Schäfers, W. Braun, W. Eberhardt, Eur. Phys. J. Special Topics, **169**, 221-225 (2009)

[14] J. J. Yeh, I. Lindau, Atomic Data and Nuclear Data Tables, **32**, 1-155 (1985)

[15] M.B. Trzhaskovskaya, V.I. Nefedov, V.G. Yarzhemsky, Atomic Data and Nuclear Tables **77**, 97-159 (2001)

[16] H. Junge, N. Marquet, A. Kammer, S. Denurra, M. Bauer, S. Wohlrab, F. Gärtner, M.-M. Pohl, A. Spannenberg, S. Gladiali, M. Beller, Chem. Eur. J., **18** 12749-12758 (2012)

[17] C.T. Au, M.W. Roberts, Chem. Phys. Lett. **74**, 472-474 (1980)

[18] M.W. Roberts, Pure & Appl. Chem., **53**, 2269-2281 (1981)

[19] I.M., Kodintsev, S. Trasatti, M. Rubel, A. Wieckowski, N. Kaufher, Langmuir, **8**, 283-290 (1992)

[20] W.N. Delgass , T.R. Hughes, C.S.Fadley, Cat. Rev.: Sci Eng., **4**, 179-220 (1971)

[21] K.S. Kim, N. Winograd, R.E. Davis, J. Am. Chem. Soc., **93**, 6296-6297 (1971)

[22] G.C. Allen, P.M. Tucker, A. Capon, R. Parsons, Electroanal. Chem. Inter. Electrochem., **50** 335-343 (1974)

[23] J.S. Hammond, N. Winograd, J. Electroanal. Chem., **78** 55-69 (1977)

[24] M. Peuckert, H.P. Bonzel, Surface Science Lett., **145** A372 (1984)

[25] M. Peuckert, Surface Science, **144** 451-464 (1984)

[26] J.B. Goodenough, A. Hamnett, B.J. Kennedy, R. Manohran, S.S. Weeks, J. Electroanal. Chem., **240** 133-145 (1984)

[27] L. Atanasoska, R. Atanasoski, S. Trasatti, Vacuum, **40**, 91-94 (1990)

[28] G. Lalande, M. C. Denis, D. Guay, J.P. Dodelet, R. Schulz, J. Alloys and Comp., **292** 301-310 (1999)

[29] B. Yang, Q. Lu, Y. Wang, L. Zhuang, J. Lu, P. Liu, Chem. Mater., **15** 3552-3557 (2003)

[30] N. Smith, G. K. Wertheim, S. Hüfner, M. M. Traum, Phys. Rev. B, **10**, 3197-3206 (1974)

[31] S. Tanuma, C. J. Powell, D. R. Penn, Surf. Interf. Anal. **21** 165 (1994)

[32] L. K. Ono, J. R. Croy, H. Heinrich, B. Roldan Cuenya, J. Phys. Chem. C, **115** 16856-16866 (2011)

[33] E. H. P. Cordfunke, Thermochimica Acta, **50**, 177-185 (1981)